This is an open access article published under an ACS AuthorChoice License, which permits copying and redistribution of the article or any adaptations for non-commercial purposes.

ACS OMEGA

Article

Cite This: ACS Omega 2019, 4, 13465−13473

http://pubs.acs.org/journal/acsodf

Carbon Derived from Soft Pyrolysis of a Covalent Organic Framework as a Support for Small-Sized RuO_2 Showing Exceptionally Low Overpotential for Oxygen Evolution Reaction

Debanjan Chakraborty,[†] Shyamapada Nandi,[†] Rajith Illathvalappil,[§] Dinesh Mullangi,[†] Rahul Maity,[†] Santosh K. Singh,[§] Sattwick Haldar,[†] Chathakudath P. Vinod,[∥] Sreekumar Kurungot,*[,§] and Ramanathan Vaidhyanathan*[,†,‡]

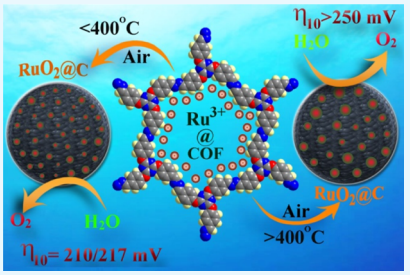
[†]Department of Chemistry and [‡]Centre for Energy Science, Indian Institute of Science Education and Research, Pune 411008, India

[§]Physical and Materials Chemistry Division, CSIR-National Chemical Laboratory, Pune 411008, India

[∥]CSIR−NCL Catalysis and Inorganic Chemistry Division, Pune 411008, India

Supporting Information

ABSTRACT: Electrochemical water splitting is the most energy-efficient technique for producing hydrogen and oxygen, the two valuable gases. However, it is limited by the slow kinetics of the anodic oxygen evolution reaction (OER), which can be improved using catalysts. Covalent organic framework (COF)-derived porous carbon can serve as an excellent catalyst support. Here, we report high electrocatalytic activity of two composites, formed by supporting RuO_2 on carbon derived from two COFs with closely related structures. These composites catalyze oxygen evolution from alkaline media with overpotentials as low as 210 and 217 mV at 10 mA/cm^2, respectively. The Tafel slopes of these catalysts (65 and 67 mV/dec) indicate fast kinetics compared to commercial RuO_2. The observed activity is the highest among all RuO_2-based heterogeneous OER catalysts—a touted benchmark OER catalyst. The high catalytic activity arises from the extremely small-sized (∼3−4 nm) RuO_2 nanoparticles homogeneously dispersed in a micro-mesoporous (BET = 517 m^2/g) COF-derived carbon. The porous graphenic carbon favors mass transfer, while its N-rich framework anchors the catalytic nanoparticles, making it highly stable and recyclable. Crucially, the soft pyrolysis of the COF enables the formation of porous carbon and simultaneous growth of small RuO_2 particles without aggregation.



1. INTRODUCTION

Covalent organic framework (COF)-derived carbons can be highly structured with substantial surface areas.[1−9] This makes them good supports for the catalyst/electrocatalyst.[7−9] The mesopores in the COF can accommodate active nanoparticles.[10−15] Of the different approaches to developing COFs as supports for electrocatalytic nanoparticles,[16−21] utilizing them as a single-source precursor for generating nitrogen-functionalized (pyridinic, pyrollic, etc.) porous carbons is quite effective. Such carbons can have high surface areas,[22] and the N- and the C-centers in their framework can provide appropriate binding sites for the catalytically active metal, and their inherent micro-mesoporosity favor high active-site accessibility and mass transfer via shortened diffusion paths. Most importantly, if the carbons can be synthesized from the framework solids using mild conditions (T < 500 °C), they can be expected to have less microstructural defects and potential high carbon-electrolyte interfacial energy.[23−26] This makes them superior to typical amorphous carbons obtained from high-temperature pyrolysis.[27−29]

Catalyzed electrochemical oxygen evolution reaction (OER) involves the release acceptance of the electron and proton.[30,31] However, most catalysts display torpid kinetics, making water-splitting less translatable in practice.[30,32] Developing highly active and durable OER catalysts can make the technology lucrative.[30,33−41] Their performance is normally quantified by overpotential (η), the extra voltage required over the thermodynamic potential (1.23 V) for the 4e-process. Most OER catalysts are oxide-based and require >300 mV overpotential (η_{10}) to deliver 10 mA/cm^2 of geometrical current density.[30,42−44] Only a countable number of them manifests <250 mV overpotential to reach a current density of 10 mA/cm^2 (see Table S1).[16,19,30,40,45−48] Precious metal oxides such as IrO_2 and RuO_2 are known to catalyze OER effectively.[30,49−51] Though precious metals can easily be ruled out as an expensive choice for an OER catalyst, their superior performance still makes them promising.[52,53] For these to reach realistic applications, their concentrations in the active catalyst need to be kept low, the catalyst need to be recyclable, and the catalyst support has to be cheap. Most importantly, if such expensive catalysts can be made to run for long cycles, the cost may not be a huge factor over extended operation periods.

Received: June 15, 2019
Accepted: July 25, 2019
Published: August 9, 2019

© 2019 American Chemical Society

DOI: 10.1021/acsomega.9b01777
ACS Omega 2019, 4, 13465−13473

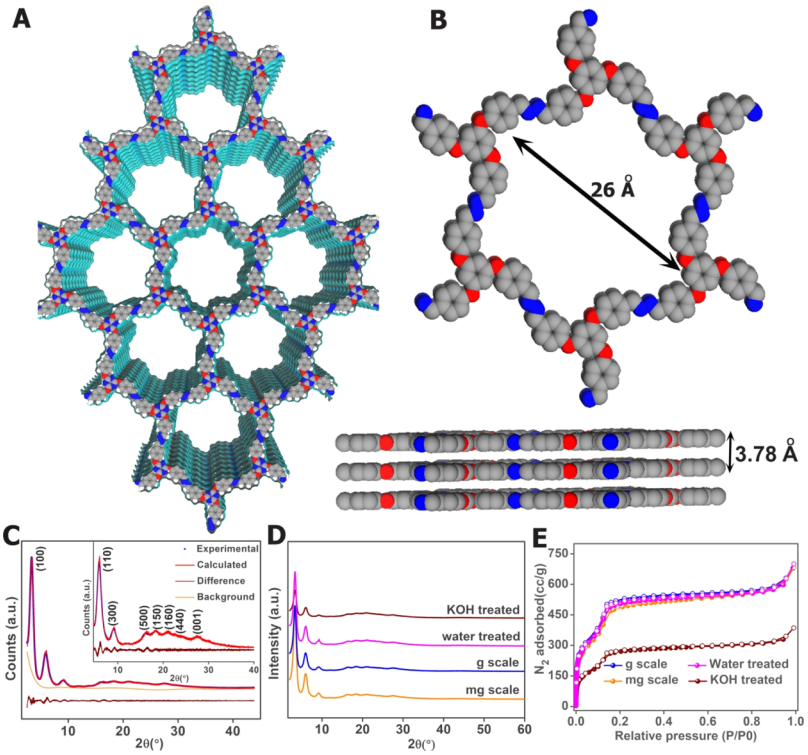


Figure 1. (A) Connolly representation of the structure of IISRP-COF6 showing the presence of uniform hexagonal channels. (B) Mesopores in IISRP-COF6 and their AAA···stacking with optimal interlayer separation for $\pi-\pi$ interactions. Color code: C-gray; N-blue; O-red. (C) Pawley fit for IISERP-COF6. (D) Scalability and stability of IISERP-COF6 from powder X-ray diffraction. (E) Porosity comparisons of the samples refluxed in water and soaked in KOH (1 M, 12 h).

These advantageous features are the hallmark of a heterogeneous catalyst. In many works, the OER catalysts are benchmarked against Ru- and Ir-based ones.[38,47−55] However, a scrutiny of the literature reveals that the touted Ru containing heterogeneous catalysts using different carbonaceous and metal foam supports have high overpotentials for OER particularly under alkaline conditions (Table S1).[54−58] This leaves a clear missing piece. What is the best performance achievable from the heterogeneous Ru-based OER catalyst?

Our study identifies a soft pyrolysis method that supports the formation of two materials that require contrasting synthesis conditions. Formation of RuO_2 nanoparticles requires the use of surfactants and annealing under oxidizing conditions. However, even 500 °C is known to cause significant growth of RuO_2 nanoparticles (~6 nm).[59] Meanwhile, the synthesis of graphenic carbon supports from various sources including COFs generally requires temperatures >600 °C. Thus, identifying soft chemical routes to synthesize these carbons under conditions that favor the growth of small metal-derived nanoparticles can be of immense value. Here, we have utilized the COF as a sacrificial reaction pot for the growth of RuO_2 under mild annealing temperatures (<400 °C). Our approach yields a homogeneous dispersion of RuO_2 in ordered micro-mesoporous N-rich carbons derived from two different N-rich COFs with related structures. RuO_2 grow as extremely small-sized nanoparticles (~3−4 nm). The RuO_2@C composites catalyze OER with a η_{10} of only 210 and 217 mV in alkaline medium. The overpotentials observed for these composites are very close to the recently reported high-performing (191 and 200 mV) electrocatalysts,[38] wherein the elevated activity emerge only upon supporting the catalyst on highly conducting nickel−gold foam as against the all-organic carbon host presented here.

2. RESULTS AND DISCUSSION

2.1. Synthesis and Structure of the IISERP-COF6. IISERP-COF1 (1) was prepared according to our earlier reported procedure[17] with slight modification to the solvent combination. IISERP-COF6 (2), reported here for the first time, was synthesized by reacting 1,3,5-triazine-2,4,6-triyltris-(oxy))tribenzaldehyde and hydrazine hydrate in a mixture of mesitylene, *ortho*-dichlorobenzene (ODCB), and ethanol (EtOH) in a sealed Pyrex tube under solvothermal conditions (90 °C for 3 days) (Scheme S1).

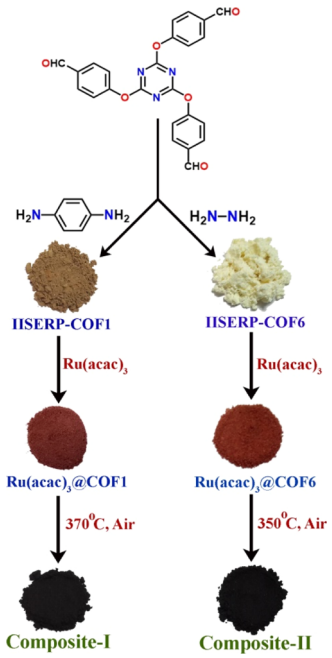
We described the structure of IISERP-COF1 (1) elsewhere.[17] Similar to 1, IISERP-COF6 (2) also has a 2D hexagonal honeycomb structure (Figure 1A). The structures of the COFs were solved employing crystal building simulations and periodic DFT-based geometry optimizations using the Material Studio program. The structure was geometry-optimized using tight binding density functional theory (DFTB). In the optimized structure of 2, the layers stack in an AAA···fashion, generating hexagonal-shaped pores with a diameter of 26.0 Å along the ab-plane (Figures 1B and S1, not factoring the van der Waals radii). The powder X-ray diffraction pattern (PXRD) for 2 was refined in the *P6/m* space group using the Pawley routine, which yielded an excellent fit. Refined cell parameters: $a = b = 31.395(5)$; $c = 3.386(7)$; $R_p = 3.77\%$; $wR_p = 5.1\%$ (Figure 1C). The COF forms pure as confirmed from their PXRD patterns (Figure 1C). The COF retains its crystallinity even after being exposed to basic conditions (1 M KOH, 12 h, Figure 1D). From 77 K N_2 adsorption−desorption isotherms, the Brauner−Emmett−

DOI: 10.1021/acsomega.9b01777
ACS Omega 2019, 4, 13465−13473

Teller (BET) surface area of 1290 and 1440 m^2/g was estimated for 1 and 2, respectively.[17] A model-independent Barrett–Joyner–Halenda (BJH) fit to the desorption branch yields pore sizes of 25 Å for 1 and 23 Å for 2. A ∼40% drop in the porosity of 2 is observed when it is treated with KOH (Figure 1E).

2.2. Synthesis and Characterizations of the COF-Derived Carbons. A family of composites was synthesized by heating 1/2 loaded with $Ru(acac)_3$ at different temperatures (250, 280, 310, and 350/370 °C). At this elevated temperatures, $Ru(acac)_3$ oxidizes, while the COFs undergo carbonization (Figure S3). The trapping of $Ru(acac)_3$ in the nanopores of the COFs helps to grow truly small-sized (<5 nm) RuO_2 nanoparticles in this capping agent-free method. The soft pyrolysis restrains RuO_2 from growing into larger particles. We have used the COF, as they are known to pyrolyze to high surface area carbons with accessible porosity.[22] The best-performing catalysts were IISERP-COF1_RuO_2@370 (Composite-I) and IISERP-COF6_RuO_2@350 (Composite-II); they are mostly discussed here (Scheme 1).

Scheme 1. Schematic Representation of the Entire Process of the Catalyst Preparation



From the PXRD patterns and the thermogravimetric analysis (TGA) plots of the pyrolysis products, we find that the complete carbonization of the RuO_2-loaded COF occurred at 350–370 °C (Figures S4–S7). The COF pyrolysis was carried out in the absence of RuO_2 to establish the nature of the carbon that was produced. We noticed that the resulting carbon was micro-mesoporous with high surface areas (BET = 517 m^2/g; Langmuir: 840 m^2/g; BJH pore size: 27 Å). A DFT fit (C-spherical pore model) indicates the presence of hierarchical pores. Notably, this was found to be graphenic carbon with a significantly ordered structure as confirmed by PXRD and Raman (Figures S8 and S9). Formation of such graphenic carbon from tartaric acid at these temperatures (<400 °C) is known,[60] but we reproduced this by carrying out the pyrolysis of tartaric acid at 370 °C and found that the resulting graphenic carbon was nonporous (Figure S10). These observations emphasize the importance of having to use the COF as a single source precursor for generating porous graphenic carbons.

The fluffy needle-shaped morphology of the carbons was very similar to those of the respective parent COFs as can be seen from the field emission scanning electron microscopy (FESEM) images (Figure 2). The elemental mapping confirms the homogeneity of the Ru distribution in both the composites (Figures S11–S40). A comparison of the adsorption isotherms of the composites prepared at different temperatures reveals a systematic drop in the porosity with increasing temperature (Figure 2).

From the high-resolution transmission electron microscopy (HRTEM) images, the majority of the RuO_2 particles are in the size limit of ∼2.5–4 nm (Figures 2 and S41). SAED patterns of the composites reveal their poor long-range crystallinity (Figures S42 and S43), yet there are crystalline regions giving rise to lattice fringes. The indexing of the lattice fringes from the HRTEM shows that the different crystal facets corresponding to the [200], [101], and [110] reflections of the tetragonal RuO_2 (ICDD: 00-040-1290) are exposed in the composites (Figure 2F,L). Some of these facets are known to be highly active for OER.[52,53,59]

Interestingly, the Raman and infrared spectra (IR) (Figures S44–S47) showed that the many of the functionalities of the COF were nearly intact in this soft pyrolysis-generated carbon. The aforementioned fact corroborates well with the large C/N ratio (neat COF = 3; RuO_2@C = 4.25) obtained from the elemental analysis. The Raman spectra show the characteristic graphenic D and G band being present in this carbon (Figure S47). To verify the electronic conductivity of this graphenic composite, we carried out four-probe measurements. The conductivity of IISERP-COF1_RuO_2@370 was 2×10^{-5} S/cm (Figure S48), which is quite moderate compared to the traditional graphenic carbon (∼103 S/cm) synthesized at high temperatures (>800 °C).[61,62] This means we do not get any major advantage of electronic modulation from this COF-derived carbon support.[19]

The X-ray photoelectron spectroscopy (XPS) analyses on IISERP-COF1_RuO_2@370 reveal the presence of characteristics peaks for RuO_2 (Figure S67, Ru $^3p_{1/2}$: 485.0 eV and Ru $^3p_{3/2}$: 462.9 eV).[63] In the C 1s spectra, the peak at 280.9 corresponds to RuO_2, and the peak at 282.5 eV is assignable to RuO_3, occurring as a surface defect.[64,65] The other higher binding energy peaks can be assigned to C 1s 285 and 287. N 1s spectra have two features of note. The peaks at 399.4 and 400.7 eV signify the presence of pyridinic and pyrrolic nitrogen in the carbon framework, and these are positively shifted, potentially from weak Ru–N interactions.[66] O 1s spectra show the presence of a peak at 532.2 eV which corresponds to Ru–O bonds.[63] This was consistent with the 459 and 506 cm^{-1} bands observed in the IR spectra (Figure S46), which is assigned to the Ru–N and Ru–O stretching frequency.[67,68]

2.3. Electrochemical Measurements. Electrochemical measurements were carried out using a traditional three-electrode setup using Hg/HgO and platinum flag as the reference, counter, and catalyst-coated glassy carbon as a working electrode, respectively. All potentials measured by using Hg/HgO were converted into the reversible hydrogen electrode (RHE) scale by calibrating Hg/HgO in 1 M KOH solution, saturated with H_2. The catalyst mass loading was maintained to be 5 μg for all electrochemical studies. There

DOI: 10.1021/acsomega.9b01777
ACS Omega 2019, 4, 13465–13473

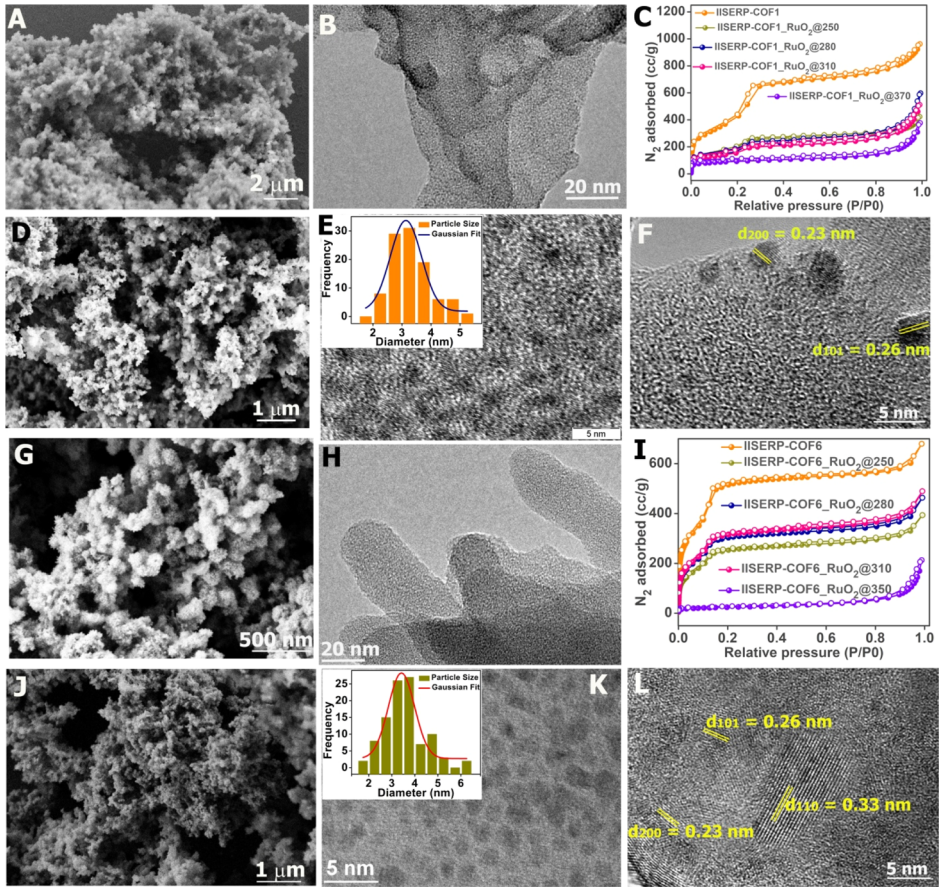


Figure 2. (A) FESEM Images of IISERP-COF1. (B)TEM images of IISERP-COF1 (C) N_2 sorption at 77 K of IISERP-COF1 and RuO_2-loaded IISERP-COF1. (D) FESEM image of IISERP-COF1_RuO_2@370. (E) TEM Images of IISERP-COF1_RuO_2@370. (F) HRTEM image of IISERP-COF1_RuO_2@370 showing the lattice fringes. (G) FESEM Images of IISERP-COF6. (H)TEM images of IISERP-COF6 (I) N_2 sorption at 77 K of IISERP-COF6 and RuO_2-loaded IISERP-COF6. (J) FESEM image of IISERP-COF6_RuO_2@350. (K) TEM Images of IISERP-COF6_RuO_2@350. (L) HRTEM image of IISERP-COF6_RuO_2@350 showing the lattice fringes. B and H show the presence of uniform micropores all along the surface of the COFs.

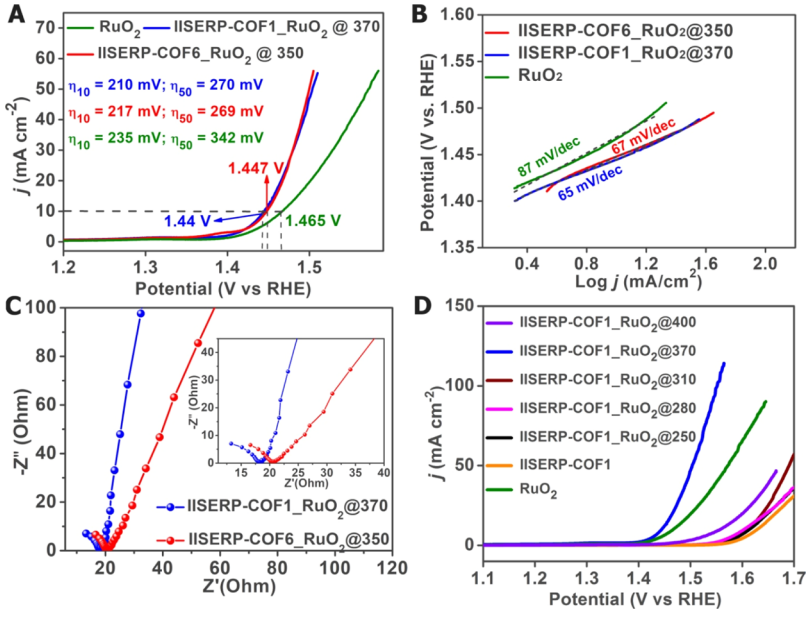


Figure 3. (A) LSV curves showing the overpotentials for composites prepared from IISERP-COF1 and IISERP-COF6. (B) Comparison of the Tafel slope for composite-I and composite-II. (C) Nyquist plots showing the resistivity for composite-I and composite-II. (D) Comparative LSV plots for composite-I showing the systematic increase in activity with the increase in their synthesis temperature. This is related to the controlled formation of graphenic carbon.

DOI: 10.1021/acsomega.9b01777
ACS Omega 2019, 4, 13465−13473

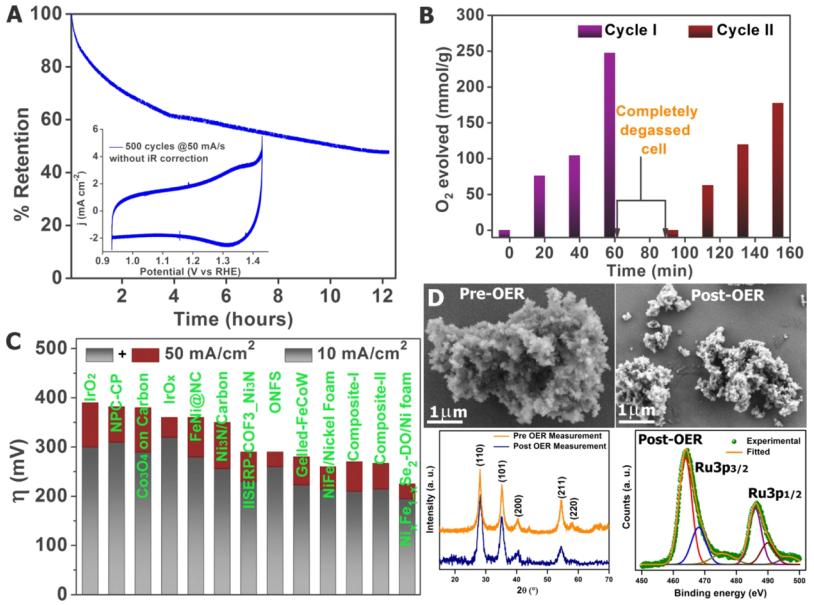


Figure 4. (A) Chronoamperometry plot showing moderate stability in the current outputs over 12 h. Inset: the Ru(IV)−Ru(V) redox couple in composite-I showing stability over 500 CV cycles. (B) Quantification of the evolved oxygen from GC over two subsequent cycles. (C) Comparison of overpotential for composite-I and composite-II with some of the top performing OER catalyst. (D) FE-SEM, PXRD, and XPS characterizations of the spent catalyst.

was a sharp rise in current after 1.4 V due to the oxygen evolution. The onset potentials for composite-I and composite-II were 1.37 and 1.38 V, respectively. The overpotentials (η) at a current density of 10 mA/cm^2 calculated for composite-I and composite-II were 210 and 217 mV, respectively, (Figure 3A) which is to the best of our knowledge is the lowest reported overpotential for a RuO_2 catalyst till date.

The overpotentials to achieve a current density of 50 mA/cm^2 for composite-I and composite-II were 274 and 269 mV, respectively, which are quite remarkable. Not only the low overpotential but these composites also deliver current density as high as 200 mA/cm^2 at a potential of only 1.6 V which is highly desirable for faster kinetics. From a plot of log I versus potential, the Tafel slope (with 65% IR-compensation) was calculated for composite-I and composite-II to be 65 and 67 mV/dec, respectively (Figure 3B), which indicates trouble-free mass and charge transfer at the electrode and electrolyte contact yielding fast kinetics for OER. Electrochemical impedance spectra comparisons show that composite-I has less resistance than composite-II (Figure 3C).

As composite-I has better performance as composite-II (Figure 3A,D), the electrochemical stability studies were carried out with Composite-I. Highly reproducible loops over continuous 500 CV cycle measurements at 50 mV/s in the Faradaic region (1−1.4 V, Figure 4A) confirmed Composite-I's cyclic stability. The cyclic voltammetry (CV) profile indicates well-featured redox peaks in the cathodic and anodic scans, corresponding to the Ru(IV)−Ru(V) redox couple. The characteristic features of the CV profile in the first cycle were completely intact even after 500 cycles. Also, there was some small contribution from the capacitive current in the non-Faradaic region. To further establish the electrochemical stability of the composite, chronoamperometry measurements were carried out. A moderately stable current was generated over 12 h (Figure 4A). The Faradaic efficiency of the composite was calculated from the rotating ring-disk electrode experiment carried out by applying a series of current (Figure S68). Faradaic efficiency for composite-I was evaluated to be 98% at 0.25 mA which further systematically reduces to 25% at 2.65 mA disc current. This reduction in Faradaic efficiency at higher current was due to the rapid release of oxygen at the disc electrode, and all of which do not get collected on the ring, as some escapes. The same is the cause for the drop in the activity during the chronoamperometry, something we noticed consistently during multiple measurements. In more detail, the decline could occur due to two possibilities, either RuO_2 leaches out from the COF or RuO_2@C shows poor adhesion with the electrode. To test this, we carried out the experiment with a larger electrode and with a larger sample, and then, we collected the postcatalysis sample and measured the PXRD which showed RuO_2 being intact in the carbon (Figure 4). Thus, it appears that the rapid evolution of oxygen witnessed by the vigorous bubbling most likely weakens the adherence of RuO_2@C with the electrode. This disintegration of the catalyst from the electrode due to rapid oxygen bubbling could represent a practical problem for all high activity materials and this leaves sufficient room for the optimization of the material/electrode preparation.

As another realistic estimation of the catalyst efficiency, we quantified the oxygen evolved during the OER. A systematic increase of the oxygen amount from 0 to 248 mmol/h/g was observed (Figure 4B); this is higher than the amounts reported for other COF nanoparticle-based OER catalysts.[16,19,69] Cyclic stability was confirmed by repeating the same experiment. Each time, before the measurement, the cell was fully degassed for 1 h. Some drop in the oxygen amount in the second cycle is due to the bubble formation at the electrode surface. Despite this, the superior performance of the composites compared to many top-performing OER catalysts can be seen from Figure 4C. Composite-I had good structural integrity under these electrochemical conditions (1 M KOH, 1−1.6 V, 500 cycles), which was confirmed by PXRD, scanning electron microscopy (SEM), and XPS studies (Figures 4D and S69−S71). Notably, the presence of Ru-3p peaks (Ru $^3p^{1/2}$: 489.9 eV and Ru $^3p_{3/2}$:

DOI: 10.1021/acsomega.9b01777
ACS Omega 2019, 4, 13465−13473

463.8 eV) in the spent catalyst means, at the end of the redox cycles, RuO_2 is recovered.

The TOF for the OER was calculated to be 0.103 at 300 mV for composite-I. This TOF is notably higher than the neat RuO_2,[50] RuO_2@CN*x*,[50] and Ir/C[58] but is lower than some of the Fe-based amorphous catalysts[38,39,45] and the recently reported Ni_3N-COF19-based catalyst (Figures S72, S73, and see Table S3). However, we do see a more vigorous evolution in this case, which is explained by the superior kinetics (Tafel slopes: 65 mV/decade for composite-I). The observed kinetics is inferior only to Gelled FeCoW oxy-hydroxide[38] and $Fe(PO3)_2/Ni_2P$.[45] A comparison of the OER overpotentials for selected high-performing materials with our composites at current densities of 10 and 50 mA/cm^2 is shown in Figure 4C and listed in Table S1. The superiority of the performance of this composite originates not only from the small-sized RuO_2 nanoparticles grown at a precise temperature (Figures 2, 3D, S41, and S74−S78) but also from the high degree of crystallinity evidenced from the lattice fringes arising from the stacked structure of the graphitic sheets (Figure S8), quite comparable to the recently reported COF-derived carbons.[9]

3. CONCLUSIONS

To summarize, we have developed a heterogeneous RuO_2-based OER catalyst using the soft-pyrolysis method by employing the COF as a sacrificial precursor in open air. This favors the growth of small-sized RuO_2 nanoparticles in the nanoconfinement of porous graphenic carbon. This brings both energy benefits and opens up the possibility of making superior catalysts via soft pyrolysis of the COF. Considering that ruthenium compounds are the benchmark catalysts for OER, the performance reported for this new RuO_2 catalyst clearly raises the bar.

4. EXPERIMENTAL SECTION

4.1. Synthesis. All chemicals were purchased from Sigma-Aldrich and used without further purification. 4,4′,4″-((1,3,5-triazine-2,4,6-triyl)tris(oxy))tribenzaldehyde was synthesized according to the reported procedure.[70]

4.1.1. Synthesis of IISERP-COF1. This was synthesized via reported procedure S2 with slight modification. In a 20 ml pyrex tube, 0.112 g (0.25 mmol) of 4,4′,4″-((1,3,5-triazine-2,4,6-triyl)tris(oxy))tribenzaldehyde and 0.044 g (0.4 mmol)-1,4-phenylenediamine were dissolved in a mixture of 3 mL Mesitylene, 3 mL ODCB, and 5 mL EtOH. The mixture was then stirred at room temperature for 60 min. During stirring, off-white colored slurry was formed. About 0.3 mL of aqueous acetic acid (6 M) was added to this slurry, and contents were stirred for another 30 min. The tube was then purged with N_2 and flash frozen in liquid nitrogen. Then, the tube was sealed under a blanket of nitrogen and heated to 120 °C for 3 days in a programmable oven. When the reaction mixture was cooled to room temperature, an off-white colored fluffy powder was obtained, which was isolated by vacuum filtration. The product was subjected to vigorous washing with dimethylformamide (DMF), dimethylacetamide (DMA), acetone, and finally with plenty of tetrahydrofuran (THF). It was dried in hot air oven before further characterization. The yield was 76% with respect to the aldehyde. Formula: $C_{66}N_{12}O_6H_{30}$; molecular weight: 1087.04 g/mol. CHN values (calculated values within bracket): C: 68.2 (72.92%); H: 4.18 (2.78%); N: 16.06 (15.46%). Note that the COF utilizing these monomers are highly reproducible, and many COFs are being reported by other groups using this trialdehyde monomer since our first report of IISERP-COF1.[17]

4.1.2. Synthesis of IISERP-COF6. In a 20 mL pyrex tube, 4,4′,4″-((1,3,5-triazine-2,4,6-triyl)tris(oxy))tribenzaldehyde 0.112 g (0.25 mmol) was dissolved in a mixture of 3 mL mesitylene, 3 mL orthodichlorobenzene (ODCB), and 5 mL EtOH. Following this, hydrazine hydrate (35%) 0.03 mL was added to the mixture under vigorous stirring at room temperature. Contents were stirred for 60 min. During stirring, off-white colored slurry was formed. About 0.25 mL of aqueous acetic acid (6 M) was added to the mixture and stirred for another 30 min. The tube was then purged with N_2 and flash frozen in liquid nitrogen. Then, the tube was sealed under a blanket of nitrogen and heated to 90 °C for 3 days in a programmable oven. After the reaction mixture was cooled to room temperature, the product, an off-white colored fluffy powder, was isolated by vacuum filtration. It was subjected to vigorous washing with DMF, DMA, acetone, and finally with plenty of THF. It was dried in a hot air oven before further characterization. The yield was 78% with respect to the aldehyde. Formula: $C_{48}N_{12}O_6$ H_{30}; molecular weight: 870.842 g/mol. CHN values (calculated values within bracket): C: 66.61(66.20); H: 3.87 (3.47); N: 20.29 (19.30). This is a cost-effective COF and forms reproducibly in good yields and is quite crystalline. The discrepancies in the calculated and observed CHN values most likely stem from the guest solvent molecules in the pore and the presence of some unreacted terminal aldehydes. These are consistent with the observations from the TGA and the ^{13}C-SSNMR.

4.1.3. Synthesis of IISERP-COF1_RuO$_2$@370. The synthesis of IISERP-COF1_RuO_2 was carried out in two steps. A solution of $Ru(acac)_3$ (100 mg) in 10 mL of MeOH was slowly added to a sonicated suspension of IISERP-COF1 (250 mg) in 50 mL THF. After the inorganics addition, the mixture turned to a bright pink color, and it was allowed to stir for 24 h at room temperature. Following this, the suspension was allowed to settle down, and the solid was recovered by centrifugation. This solid was thoroughly washed with THF and MeOH [note that $Ru(acac)_3$ is highly soluble in these solvents]. Thus, isolated pink-colored solid, Ru(acac)3 loaded in COF, was heated at 370 °C for 3 h under air. After cooling to room temperature, the black powder was collected. CHN values: C: 74.64%; H: 1.61%; N: 8.84%.

4.1.4. Synthesis of IISERP-COF6_RuO$_2$@350. The synthesis of IISERP-COF6_RuO_2 was carried out in two steps. A solution of $Ru(acac)_3$ (100 mg) in 10 mL of MeOH was slowly added to a suspension of IISERP-COF6 (250 mg) in 50 mL THF. After this inorganics addition, the mixture turned from a yellow suspension to a bright pink color. It was allowed to stir for 24 h at room temperature. Following this, the suspension was allowed to settle down, and the solid was recovered by centrifugation and washed. The pink-colored solid, $Ru(acac)_3$ loaded in COF was the heated at 350 °C for 3 h under air. When cooled to room temperature, a homogeneous black powder was obtained. This was washed vigorously with water, methanol, and THF. No colored compounds were seen in the postwash solutions. CHN values: C: 75.52%; H: 0.57%; N: 7.66%.

4.1.5. Synthesis of IISERP-COF1@370. To verify the role of COF-derived carbon in the synthesis, IISERP-COF1 was pyrolyzed at 370 °C under air. The black powder was washed with water, THF, and methanol. CHN values: C: 59.77%; H:

DOI: 10.1021/acsomega.9b01777
ACS Omega 2019, 4, 13465−13473

1.86%; N: 14.54%. Note that the presence of substantial quantities of nitrogen in these carbons is generated from COF pyrolysis.

Note that the optimal pyrolysis temperature for the preparation of a homogeneous carbon-supported RuO_2 catalyst was established from systematic analysis using the PXRD and TGA (Figures S4–S7). The pyrolysis temperature was chosen based on the decomposition temperatures of the COF.

4.2. Analytical Characterizations. *4.2.1. Powder X-Ray Diffraction.* Powder XRD was carried out using a full-fledge Bruker Pxrd instrument. In some cases, the data were recorded using a Rigaku Miniflex-600 instrument and processed using PDXL software.

4.2.2. Thermogravimetric Analysis. Thermogravimetry was carried out on the NETSZCH TGA–DSC system. The routine TGAs were carried out under N_2 gas flow (20 mL/min) (purge + protective), and samples were heated from 25 to 550 °C at 4 K/min.

4.2.3. IR Spectroscopy. IR spectra were obtained using a Nicolet ID5-attenuated total reflectance IR spectrometer operating at ambient temperature. The KBr pellets were used for IR data collection.

4.3. Field Emission SEM. FESEM images were collected using the Ultra Plus field emission scanning electron microscope with the integral charge compensator and embedded EsB and AsB detectors. Oxford X-max instruments 80 mm^2. (Carl Zeiss NTS, Gmbh), Imaging conditions: 2 kV, WD = 2 mm, 200 kX, Inlens detector. For SEM images, as an initial preparation, the samples were ground thoroughly, soaked in THF for 30 min, and were sonicated for 5 min. These well-dispersed samples were drop-casted on a silicon wafer and dried under vacuum for 12 h.

4.3.1. High-Resolution Transmission Electron Microscopy (HRTEM). The FEI (Jeol FEG 2100F is the model) high-resolution transmission electron microscope (HR-TEM) equipped with a field emission source operating at 300 KeV was used.

4.3.2. Adsorption Studies. All adsorption studies were carried out using a 3-FLEX pore and surface area analyzer, micromeritics and few cases "Autosorb IQ", Quantachrome.

4.3.3. X-ray Photoelectron Spectroscopy (XPS). XPS measurements were carried out using the Thermo K alpha + spectrometer using microfocused and monochromated Al Kα radiation with an energy of 1486.6 eV. The base pressure of the instrument was 1×10^{-9} Torr. The pass energy for spectral acquisition was kept at 50 eV for individual core levels. The electron flood gun was utilized for providing charge compensation during data acquisition. The peak fitting of the individual core levels was done using Origin Pro software with a Shirley-type background.

4.4. Electrochemical Measurements. The electrochemical measurement was carried out using a Bio-Logic instrument with techniques such as CV, linear sweep voltammetry (LSV), and chronoamperometry. Typically, a three-electrode test cell was fabricated using Hg/HgO and platinum flag as the reference and counter electrode, respectively. The catalyst-coated glassy carbon electrode was used as the working electrode.

4.4.1. Preparation of Working Electrode. This was prepared by coating the catalyst on the carbon disk and with subsequent drying under an IR lamp. The catalyst mass loading was maintained to be 5 μg for all electrochemical studies.

4.4.2. Electrolyte. For all electrochemical measurements, the degassed 1 M KOH was used as the electrolyte. All potentials were converted to RHE according to the following equation

$$E_{RHE} = E_{Hg/HgO} + 0.098 + 0.0591 \times pH$$

4.4.3. iR Correction. Excluding the resistances arising from the electrolyte, reference and counter electrodes are necessary. For this, *iR* compensation needs to be done on the LSV data. However, excluding the electrolyte resistance completely from the system is not realistic. This is due to internal resistance from the electrochemical system. In this study, we have corrected the LSV data using 65% *iR* compensation. The Tafel plot is derived from the LSV data, which is already *iR* compensated.

4.4.4. Evolved Oxygen Quantification Setup. The testing was carried out in an air-tight electrochemical cell. A chronoamperometric study at 1.44 V (vs RHE) followed by quantification of headspace gas by gas chromatography (GC) was carried out. This measurement was carried out over an hour via injection of the headspace gas at a 20 min time interval.

■ ASSOCIATED CONTENT

Supporting Information

The Supporting Information is available free of charge on the ACS Publications website at DOI: 10.1021/acsomega.9b01777.

Materials and methods, analytical characterization, microscopy studies, spectroscopy studies, gas sorption analysis, X-ray photoelectron spectroscopy, and electrochemical studies (PDF)

■ AUTHOR INFORMATION

Corresponding Authors

*E-mail: k.sreekumar@ncl.res.in (S.K.).
*E-mail: vaidhya@iiserpune.ac.in (R.V.).

ORCID

Santosh K. Singh: 0000-0002-3210-3640
Chathakudath P. Vinod: 0000-0001-9857-4907
Sreekumar Kurungot: 0000-0001-5446-7923
Ramanathan Vaidhyanathan: 0000-0003-4490-4397

Author Contributions

D.C. and S.N. contributed equally. The manuscript was written through contributions of all the authors. All the authors have given approval to the final version of the manuscript.

Notes

The authors declare no competing financial interest.

■ ACKNOWLEDGMENTS

We acknowledge IISER-Pune, DST-MES program, and SERB. DC thanks DST-Inspire for financial support. The authors thank Prof. R. Nandini Devi, Catalysis Division, CSIR-NCL, for helping us with the oxygen quantification experiments.

■ REFERENCES

(1) Xu, Q.; Tang, Y.; Zhai, L.; Chen, Q.; Jiang, D. Pyrolysis of Covalent Organic Frameworks: A General Strategy for Template Converting Conventional Skeletons into Conducting Microporous Carbons for High-performance Energy Storage. *Chem. Commun.* **2017**, *53*, 11690–11693.

DOI: 10.1021/acsomega.9b01777
ACS Omega 2019, 4, 13465–13473

(2) Zhang, X.; Zhu, G.; Wang, M.; Li, J.; Lu, T.; Pan, L. Covalent-organic-Frameworks Derived N-doped Porous Carbon Materials as Anode for Superior Long-life Cycling Lithium and Sodium Ion Batteries. *Carbon* **2017**, *116*, 686−694.
(3) Kim, D. J.; Yoon, J. W.; Lee, C. S.; Bae, Y.-S.; Kim, J. H. Covalent Organic Framework-derived Microporous Carbon Nanoparticles Coated with Conducting Polypyrrole as an Electrochemical Capacitor. *Appl. Surf. Sci.* **2018**, *439*, 833−838.
(4) Huang, Y.-B.; Pachfule, P.; Sun, J.-K.; Xu, Q. From Covalent-organic Frameworks to Hierarchically Porous B-doped Carbons: A Moltensalt Approach. *J. Mater. Chem. A* **2016**, *4*, 4273−4279.
(5) Kim, G.; Yang, J.; Nakashima, N.; Shiraki, T. Highly Microporous Nitrogen-doped Carbon Synthesized from Azine-linked Covalent Organic framework and Its Supercapacitor Function. *Chem.—Eur. J.* **2017**, *23*, 17504−17510.
(6) Romero, J.; Rodriguez-San-Miguel, D.; Ribera, A.; Mas-Ballesté, R.; Otero, T. F.; Manet, I.; Licio, F.; Abellán, G.; Zamora, F.; Coronado, E. Metal-functionalized Covalent Organic Frameworks as Precursors of Super Capacitive Porous N-doped Graphene. *J. Mater. Chem. A* **2017**, *5*, 4343−4351.
(7) Li, L.; Li, L.; Cui, C.; Fan, H.; Wang, R. Heteroatom-doped Carbon Spheres from Hierarchical Hollow Covalent Organic Framework Precursors for Metal- Free Catalysis. *ChemSusChem* **2017**, *10*, 4921−4926.
(8) Chen, L.; Zhang, L.; Chen, Z.; Liu, H.; Luque, R.; Li, Y. A Covalent Organic Framework-based Route to the in Situ Encapsulation of Metal Nanoparticles in N-rich Hollow Carbon Spheres. *Chem. Sci.* **2016**, *7*, 6015−6020.
(9) Xu, Q.; Tang, Y.; Zhang, X.; Oshima, Y.; Chen, Q.; Jiang, D. Template Conversion of Covalent Organic Frameworks into 2D Conducting Nanocarbons for Catalyzing Oxygen Reduction Reaction. *Adv. Mater.* **2018**, *30*, 1706330.
(10) Waller, P. J.; Gándara, F.; Yaghi, O. M. Chemistry of Covalent Organic Frameworks. *Acc. Chem. Res.* **2015**, *48*, 3053.
(11) Segura, J. L.; Mancheño, M. J.; Zamora, F. Covalent Organic Frameworks Based on Schiff-base Chemistry: Synthesis, Properties and Potential Applications. *Chem. Soc. Rev.* **2016**, *45*, 5635.
(12) Pachfule, P.; Kandambeth, S.; Díaz Díaz, D.; Banerjee, R. Highly Stable Covalent Organic Framework−Au Nanoparticles Hybrids for Enhanced Activity for Nitrophenol Reduction. *Chem. Commun.* **2014**, *50*, 3169.
(13) Ding, S.-Y.; Gao, J.; Wang, Q.; Zhang, Y.; Song, W.-G.; Su, C.-Y.; Wang, W. Construction of Covalent Organic Framework for Catalysis: Pd/COF-LZU1 in Suzuki−Miyaura Coupling Reaction. *J. Am. Chem. Soc.* **2011**, *133*, 19816.
(14) Pachfule, P.; Panda, M. K.; Kandambeth, S.; Shivaprasad, S. M.; Díaz, D. D.; Banerjee, R. Multifunctional and Robust Covalent Organic Framework−nanoparticle Hybrids. *J. Mater. Chem. A* **2014**, *2*, 7944−7952.
(15) Du, Z.-L.; Dang, Q.-Q.; Zhang, X.-M. Heptazine-Based Porous Framework Supported Palladium Nanoparticles for Green Suzuki−Miyaura Reaction. *Ind. Eng. Chem. Res.* **2017**, *56*, 4275−4280.
(16) Mullangi, D.; Dhavale, V.; Shalini, S.; Nandi, S.; Collins, S.; Woo, T.; Kurungot, S.; Vaidhyanathan, R. Low-Overpotential Electrocatalytic Water Splitting with Noble-Metal-Free Nanoparticles Supported in a sp^3 N-Rich Flexible COF. *Adv. Energy Mater.* **2016**, *6*, 1600110.
(17) Mullangi, D.; Nandi, S.; Shalini, S.; Sreedhala, S.; Vinod, C. P.; Vaidhyanathan, R. Pd Loaded Amphiphilic COF as Catalyst for Multifold Heck Reactions, C-C Couplings and CO Oxidation. *Sci. Rep.* **2015**, *5*, 10876.
(18) Stegbauer, L.; Schwinghammer, K.; Lotsch, B. V. A Hydrazone-based Covalent Organic Framework for Photocatalytic Hydrogen Production. *Chem. Sci.* **2014**, *5*, 2789.
(19) Nandi, S.; Singh, S. K.; Mullangi, D.; Illathvalappil, R.; George, L.; Vinod, C. P.; Kurungot, S.; Vaidhyanathan, R. Low Band Gap Benzimidazole COF Supported Ni_3N as Highly Active OER Catalyst. *Adv. Energy Mater.* **2016**, *6*, 1601189.
(20) Shi, X.; Yao, Y.; Xu, Y.; Liu, K.; Zhu, G.; Chi, L.; Lu, G. Imparting Catalytic Activity to a Covalent Organic Framework Material by Nanoparticle Encapsulation. *ACS Appl. Mater. Interfaces* **2017**, *9*, 7481.
(21) Mullangi, D.; Chakraborty, D.; Pradeep, A.; Koshti, V.; Vinod, C. P.; Panja, S.; Nair, S.; Vaidhyanathan, R. Highly Stable COF-Supported $Co/Co(OH)_2$ Nanoparticles Heterogeneous Catalyst for Reduction of Nitrile/Nitro Compounds under Mild Conditions. *Small* **2018**, *14*, 1801233.
(22) Pachfule, P.; Shinde, D.; Majumder, M.; Xu, Q. Fabrication of Carbon Nanorods and Graphene Nanoribbons from a Metal-organic Framework. *Nat. Chem.* **2016**, *8*, 718−724.
(23) Aricò, A. S.; Bruce, P.; Scrosati, B.; Tarascon, J.-M.; van Schalkwijk, W. Nanostructured Materials for Advanced Energy Conversion and Storage Devices. *Nat. Mater.* **2005**, *4*, 366−377.
(24) Salunkhe, R. R.; Tang, J.; Kamachi, Y.; Nakato, T.; Kim, J. H.; Yamauchi, Y. Asymmetric Supercapacitors Using 3D Nanoporous Carbon and Cobalt Oxide Electrodes Synthesized from a Single MetalOrganic Framework. *ACS Nano* **2015**, *9*, 6288−6296.
(25) Yang, S.; Bachman, R. E.; Feng, X.; Müllen, K. Use of Organic Precursors and Graphenes in the Controlled Synthesis of Carbon-containing Nanomaterials for Energy Storage and Conversion. *Acc. Chem. Res.* **2013**, *46*, 116−128.
(26) Gu, W.; Yushin, G. Review of Nanostructured Carbonmaterials for Electrochemicalcapacitor Applications: Advantagesand Limitations of Activated Carbon, Carbide-derived Carbon, Zeolite-templated Carbon, Carbonaerogels, Carbon Nanotubes, Onion-like Carbon, and Graphene. *WIREs Energy Environ* **2014**, *3*, 424−473.
(27) Liu, B.; Shioyama, H.; Akita, T.; Xu, Q. Metal-organic Framework as a Template for Porous Carbon Synthesis. *J. Am. Chem. Soc.* **2008**, *130*, 5390−5391.
(28) Xia, W.; Mahmood, A.; Zou, R.; Xu, Q. Metal-organic Frameworks and Their Derived Nanostructures for Electrochemical Energy Storage and Conversion. *Energy Environ. Sci.* **2015**, *8*, 1837−1866.
(29) Sun, J.-K.; Xu, Q. Functional Materials Derived from Open Framework Templates/Precursors: Synthesis and Applications. *Energy Environ. Sci.* **2014**, *7*, 2071−2100.
(30) Suen, N.-T.; Hung, S.-F.; Quan, Q.; Zhang, N.; Xu, Y.-J.; Chen, H. M. Electrocatalysis for the Oxygen Evolution Reaction: Recent Development and Future Perspectives. *Chem. Soc. Rev.* **2017**, *46*, 337−365.
(31) (a) Seh, Z. W.; Kibsgaard, J.; Dickens, C. F.; Chorkendorff, I.; Nørskov, J. K.; Jaramillo, T. F. Combining theory and experiment in electrocatalysis: Insights into materials design. *Science* **2017**, *355*, No. eaad4998. (b) Jiang, H.; Gu, J.; Zheng, X.; Liu, M.; Qiu, X.; Wang, L.; Li, W.; Chen, Z.; Ji, X.; Li, J. Defect-rich and ultrathin N doped carbon nanosheets as advanced trifunctional metal-free electrocatalysts for the ORR, OER and HER. *Energy Environ. Sci.* **2019**, *12*, 322. (c) Thangappan, R.; Arivanandhan, M.; Dhinesh Kumar, R.; Jayavel, R. Facile synthesis of RuO_2 nanoparticles anchored on graphene nanosheets forhigh performance composite electrode for supercapacitor applications. *J. Phys. Chem. Solids* **2018**, *121*, 339−349.
(32) Cook, T. R.; Dogutan, D. K.; Reece, S. Y.; Surendranath, Y.; Teets, T. S.; Nocera, D. G. Solar Energy Supply and Storage for the Legacy and Nonlegacy Worlds. *Chem. Rev.* **2010**, *110*, 6474.
(33) Zhang, L.; Xiao, J.; Wang, H.; Shao, M. Carbon-Based Electrocatalysts for Hydrogen and Oxygen Evolution Reactions. *ACS Catal.* **2017**, *7*, 7855.
(34) Song, F.; Bai, L.; Moysiadou, A.; Lee, S.; Hu, C.; Liardet, L.; Hu, X. Transition Metal Oxides as Electrocatalysts for the Oxygen Evolution Reaction in Alkaline Solutions: An Application-Inspired Renaissance. *J. Am. Chem. Soc.* **2018**, *140*, 7748.
(35) Liu, K.; Zhong, H.; Meng, F.; Zhang, X.; Yan, J.; Jiang, Q. Recent Advances in Metal-nitrogen-carbon Catalysts for Electrochemical Water Splitting. *Mater. Chem. Front.* **2017**, *1*, 2155−2173.

DOI: 10.1021/acsomega.9b01777
ACS Omega 2019, 4, 13465−13473

(36) Galán-Mascarós, J. R. Water Oxidation at Electrodes Modified with Earth-Abundant Transition-metal Catalysts. *ChemElectroChem* **2015**, *2*, 37−50.
(37) Walter, M. G.; Warren, E. L.; McKone, J. R.; Boettcher, S. W.; Mi, Q.; Santori, E. A.; Lewis, N. S. Solar Water Splitting Cells. *Chem. Rev.* **2010**, *110*, 6446.
(38) Zhang, B.; Zheng, X.; Voznyy, O.; Comin, R.; Bajdich, M.; Garcia-Melchor, M.; Han, L.; Xu, J.; Liu, M.; Zheng, L.; Garcia de Arquer, F. P.; Dinh, C. T.; Fan, F.; Yuan, M.; Yassitepe, E.; Chen, N.; Regier, T.; Liu, P.; Li, Y.; De Luna, P.; Janmohamed, A.; Xin, H. L.; Yang, H.; Vojvodic, A.; Sargent, E. H. Homogeneously Dispersed Multimetal Oxygen-evolving Catalysts. *Science* **2016**, *352*, 333−337.
(39) Smith, R. D. L.; Prévot, M. S.; Fagan, R. D.; Zhang, Z.; Sedach, P. A.; Siu, M. K. J.; Trudel, S.; Berlinguette, C. P. Photochemical Route for Accessing Amorphous Metal Oxide Materials for Water Oxidation Catalysis. *Science* **2013**, *340*, 60−63.
(40) McCrory, C. C. L.; Jung, S.; Peters, J. C.; Jaramillo, T. F. Benchmarking Heterogeneous Electrocatalysts for the Oxygen Evolution Reaction. *J. Am. Chem. Soc.* **2013**, *135*, 16977−16987.
(41) Esiner, S.; Willems, R. E. M.; Furlan, A.; Li, W.; Wienk, M. M.; Janssen, R. A. J. Photoelectrochemical Water Splitting in an Organic Artificial Leaf. *J. Mater. Chem. A* **2015**, *3*, 23936−23945.
(42) Song, F.; Hu, H. Exfoliation of Layered Double Hydroxides for Enhanced Oxygen Evolution Catalysis. *Nat. Commun.* **2014**, *5*, 4477.
(43) Yagi, S.; Yamada, I.; Tsukasaki, H.; Seno, A.; Murakami, M.; Fujii, H.; Chen, H.; Umezawa, N.; Abe, H.; Nishiyama, N.; Mori, S. Covalency-reinforced Oxygen Evolution Reaction Catalyst. *Nat. Commun.* **2015**, *6*, 8249.
(44) Suntivich, J.; May, K. J.; Gasteiger, H. A.; Goodenough, J. B.; Shao-Horn, Y. A Perovskite Oxide Optimized for Oxygen Evolution Catalysis from Molecular Orbital Principles. *Science* **2011**, *334*, 1383−1385.
(45) Zhou, H.; Yu, F.; Sun, J.; He, R.; Chen, S.; Chu, C.-W.; Ren, Z. Highly Active Catalyst Derived from a 3D foam of $Fe(PO_3)_2/Ni_2P$ for Extremely Efficient Water Oxidation. *Proc. Natl. Acad. Sci. U.S.A.* **2017**, *114*, 5607.
(46) Jin, H.; Wang, J.; Su, D.; Wei, Z.; Pang, Z.; Wang, Y. In situ cobalt-cobalt oxide/N-doped carbon hybrids as superior bifunctional electrocatalysts for hydrogen and oxygen evolution. *J. Am. Chem. Soc.* **2015**, *137*, 2688−2694.
(47) Joya, K. S.; Ehsan, M. A.; Babar, N.-U.-A.; Sohail, M.; Yamani, Z. H. Nanoscale palladium as a new benchmark electrocatalyst for water oxidation at low overpotential. *J. Mater. Chem. A* **2019**, *7*, 9137−9144.
(48) Long, X.; Li, J.; Xiao, S.; Yan, K.; Wang, Z.; Chen, H.; Yang, S. A Strongly Coupled Graphene and FeNi Double Hydroxide Hybrid as an Excellent Electrocatalyst for the Oxygen Evolution Reaction. *Angew. Chem., Int. Ed.* **2014**, *53*, 7584−7588.
(49) Browne, M. P.; Nolan, H.; Duesberg, G. S.; Colavita, P. E.; Lyons, M. E. G. Low-overpotential High-activity Mixed Manganese and Ruthenium Oxide Electrocatalysts for Oxygen Evolution Reaction in Alkaline Media. *ACS Catal.* **2016**, *6*, 2408.
(50) Bhowmik, T.; Kundu, M. K.; Barman, S. Growth of One-Dimensional RuO_2 Nanowires on g-Carbon Nitride: An Active and Stable Bifunctional Electrocatalyst for Hydrogen and Oxygen Evolution Reactions at All pH Value. *ACS Appl. Mater. Interfaces* **2016**, *8*, 28678−28688.
(51) Mattos-Costa, F. I.; de Lima-Neto, P.; Machado, S. A. S.; Avaca, L. A. Characterisation of Surfaces Modified by Sol-gel Derived $Ru_xIr_{1-x}O_2$ Coatings for Oxygen Evolution in Acid Medium. *Electrochim. Acta* **1998**, *44*, 1515−1523.
(52) Stoerzinger, K. A.; Diaz-Morales, O.; Kolb, M.; Rao, R. R.; Frydendal, R.; Qiao, L.; Wang, X. R.; Halck, N. B.; Rossmeisl, J.; Hansen, H. A.; Vegge, T.; Stephens, I. E. L.; Koper, M. T. M.; Shao-Horn, Y. Orientation-Dependent Oxygen Evolution on RuO_2 without Lattice Exchange. *ACS Energy Lett.* **2017**, *2*, 876−881.
(53) Roy, C.; Rao, R. R.; Stoerzinger, K. A.; Hwang, J.; Rossmeisl, J.; Chorkendorff, I.; Shao-Horn, Y.; Stephens, I. E. L. Trends in Activity and Dissolution on RuO_2 under Oxygen Evolution Conditions: Particles versus Well-Defined Extended Surfaces. *ACS Energy Lett.* **2018**, *3*, 2045−2051.
(54) Yang, L.; Qi, H.; Zhang, C.; Sun, X. An Efficient Bifunctional Electrocatalyst for Water Splitting Based on Cobalt Phosphide. *Nanotechnology* **2016**, *27*, 23LT01.
(55) Dhavale, V. M.; Gaikwad, S. S.; George, L.; Devi, R. N.; Kurungot, S. Nitrogen-doped Graphene Interpenetrated 3D Ni-nanocages: Efficient and Stable Water-todioxygen Electrocatalysts. *Nanoscale* **2014**, *6*, 13179−13187.
(56) Zhao, Y.; Chen, S.; Sun, B.; Su, D.; Huang, X.; Liu, H.; Yan, Y.; Sun, K.; Wang, G. Graphene-Co_3O_4 Nanocomposite as Electrocatalyst with High Performance for Oxygen Evolution Reaction. *Sci. Rep.* **2015**, *5*, 7629.
(57) Xu, K.; Chen, P.; Li, X.; Tong, Y.; Ding, H.; Wu, X.; Chu, W.; Peng, Z.; Wu, C.; Xie, Y. Metallic Nickel Nitride Nanosheets Realizing Enhanced Electrochemical Water Oxidation. *J. Am. Chem. Soc.* **2015**, *137*, 4119−4125.
(58) Lu, X.; Zhao, C. Electrodeposition of Hierarchically Structured Three-dimensional Nickel-Iron Electrodes for Efficient Oxygen Evolution at High Current Densities. *Nat. Commun.* **2015**, *6*, 6616.
(59) Lee, Y.; Suntivich, J.; May, K. J.; Perry, E. E.; Shao-Horn, Y. Synthesis and Activities of Rutile IrO_2 and RuO_2 Nanoparticles for Oxygen Evolution in Acid and Alkaline Solutions. *J. Phys. Chem. Lett.* **2012**, *3*, 399−404.
(60) Fahmi, M. Z.; Wathoniyyah, M.; Khasanah, M.; Rahardjo, Y.; Wafiroh, S.; Abdulloh, A. Incorporation of Graphene Oxide in Polyethersulfone Mixed Matrix Membranes to Enhance Hemodialysis Membrane Performance. *RSC Adv.* **2018**, *8*, 931−937.
(61) Geim, A. K.; Novoselov, K. S. The Rise of Graphene. *Nat. Mater.* **2007**, *6*, 183−191.
(62) Wang, J.; Ma, F.; Liang, W.; Sun, M. Electrical Properties and Applications of Graphene, Hexagonal Boronnitride (h-BN), and Graphene/h-BN Heterostructures. *Mater. Today Phys.* **2017**, *2*, 6−34.
(63) Gopiraman, M.; Karvembu, R.; Kim, I. S. Highly Active, Selective, and Reusable RuO_2/SWCNT Catalyst for Heck Olefination of Aryl Halides. *ACS Catal.* **2014**, *4*, 2118−2129.
(64) Kim, K.; Winograd, N. X-Ray photoelectron spectroscopic studies of ruthenium-oxygen surfaces. *J. Catal.* **1974**, *35*, 66−72.
(65) Chan, H. Y. H.; Takoudis, C. G.; Weaver, M. J. High-Pressure Oxidation of Ruthenium as Probed by Surface-Enhanced Raman and X-Ray Photoelectron Spectroscopies. *J. Catal.* **1997**, *172*, 336−345.
(66) Zhang, J.; Liu, P.; Wang, G.; Zhang, P. P.; Zhuang, X. D.; Chen, M. W.; Weidinger, I. M.; Feng, X. L. Ruthenium/Nitrogen-Doped Carbon As an Electrocatalyst for Efficient Hydrogen Evolution in Alkaline Solution. *J. Mater. Chem. A* **2017**, *5*, 25314−25318.
(67) Khorshidi, A.; Sadeghi, N. Application of RuO_2 Nanoparticles as Catalyst in Preparation of Indolo[3,2-a]Carbazoles. *J. Clust. Sci.* **2016**, *27*, 1923−1932.
(68) Allen, A. D.; Senoff, C. V. Preparation and Infrared Spectra of Some Ammine Complexes of Ruthenium(II) and Ruthenium(III). *Can. J. Chem.* **1967**, *45*, 1337−1341.
(69) Aiyappa, H. B.; Thote, J.; Shinde, D. B.; Banerjee, R.; Kurungot, S. Cobalt Modified Covalent Organic Framework as a Robust Water Oxidation Electrocatalyst. *Chem. Mater.* **2016**, *28*, 4375−4379.
(70) Tahmassebi, D. C.; Sasaki, T. Synthesis of a New Trialdehyde Template for Molecular Imprinting. *J. Org. Chem.* **1994**, *59*, 679−681.

DOI: 10.1021/acsomega.9b01777
ACS Omega 2019, 4, 13465−13473